China Geology 9 (2026) 535−552

China Geology

Journal homepage: http://chinageology.cgs.cn
https://www.sciencedirect.com/journal/china-geology

Temperature-driven hydrate dissociation in pressure-preserved coring: A fully coupled modeling study with burst-decay kinetics

Meng Xu[a, b, c, d], Ya-chen Xie[a, c, d], Le Zhao[c, d,*], Ling Chen[a, b], Chao Yuan[c, d], Jia-liang Chen[c, d], Cheng-hang Fu[a, c, d], Han Wu[a, c, d], Gui-kang Liu[a, c, d], Ming-zhu Qi[e], Ming Zhang[f], He-ping Xie[a, b, c, d,*]

[a] *State Key Laboratory of Intelligent Construction and Healthy Operation and Maintenance of Deep Underground Engineering*, *Sichuan University*, *Chengdu* 610065, *China*
[b] *School of Mechanical Engineering*, *Sichuan University*, *Chengdu* 610065, *China*
[c] *State Key Laboratory of Intelligent Construction and Healthy Operation and Maintenance of Deep Underground Engineering*, *College of Civil and Transportation Engineering*, *Shenzhen University*, *Shenzhen* 518060, *China*
[d] *Guangdong Provincial Key Laboratory of Deep Earth Sciences and Geothermal Energy Exploitation and Utilization*, *Institute of Deep Earth Sciences and Green Energy*, *College of Civil and Transportation Engineering*, *Shenzhen University*, *Shenzhen* 518060, *China*
[e] *Shenzhen Geotechnical Investigation & Surveying Institute* (*Group*) *Company Limited*, *Shenzhen* 518028, *China*
[f] *Shenzhen Geological Science and Technology Innovation Center*, *Shenzhen* 518028, *China*

A R T I C L E I N F O

Article history:
Received 10 September 2025
Received in revised form 17 November 2025
Accepted 13 January 2026
Available online 25 February 2026

Keywords:
Natural gas hydrate
Combustible ice
Unconventional energy
Clean energy
Temperature-pressure synergistic preservation
Multiphysics coupling
Pressure-preserved coring
Hydrate dissociation kinetics
Numerical simulation
S-shaped decay

A B S T R A C T

Natural gas hydrate (NGH) extreme thermodynamic sensitivity poses challenges for pressure-preserved coring operations in reservoir evaluation and commercial development. Current preservation strategies employing "pressure-only" approaches fail to address temperature-induced instability, leading to sample degradation and compromised geological characterization. This study investigates temperature-pressure synergistic preservation mechanisms using fully coupled thermal-hydraulic-mechanical-chemical (THMC) numerical simulation of hydrate cores from the Shenhu area, South China Sea. Numerical modeling incorporating hydrate dissociation kinetics, multiphase fluid dynamics, and heat/mass transfer processes reveals that temperature variations trigger cascading destabilization mechanisms. Results demonstrate that temperature field evolution follows exponential growth patterns, generating steep radial gradients up to 35 K/cm that induce pressure surges from 0.11 MPa to 0.82 MPa, establishing positive feedback loops destabilizing hydrate structures. Hydrate dissociation kinetics conform to Kim-Bishnoi laws, exhibiting "S-shaped decay" patterns with 2 times rate acceleration under elevated temperatures, reducing dissociation completion times from 1200 s to 600 s. The investigation identifies "threshold effects" in relative permeability evolution, where growth exceeding three orders of magnitude occurs when hydrate saturation drops below 0.15–0.2, transforming core hydraulic properties. Multiphase fluid migration transitions from diffusive regimes ($0–0.4\times10^{-3}$ m/s) to explosive patterns ($1\times10^{-3}–1.25\times10^{-3}$ m/s), exhibiting "burst-decay" kinetics that compromise sample integrity through rapid methane release and pore structure reconstruction. The study establishes quantitative criteria for developing temperature-pressure synergistic preservation technologies, with numerical results indicating potential sample quality loss reduction of 60%–80%.

©2026 China Geology Editorial Office.

1. Introduction

NGH forms as cage-like crystalline structures when water and natural gas molecules combine under low-temperature, high-pressure conditions in permafrost regions and deep-sea sediments. With vast reserves and clean combustion properties, NGH represents the most promising alternative energy source for the 21st century (Sloan ED, 2003). The 2020 U.S. Geological Survey estimates that technically recoverable NGH resources exceed 3×10^{16} m^3, surpassing combined conventional and unconventional gas reserves while underscoring its strategic role in energy transition (Waite WF et al., 2020; Yu YS et al., 2021). Accurate characterization of

First author: *E-mail address*: 2023323020008@stu.scu.edu.cn (Meng Xu).

* Corresponding author: *E- mail address*: zhaole@szu.edu.cn (Le Zhao); xiehp@scu.edu.cn (He-ping Xie).

Literary editor: Xi-jie Chen
doi:10.31035/cg2025257
2096-5192/© 2026 China Geology Editorial Office.

Copyright © 2026 Editorial Office of China Geology. Publishing services by Elsevier B.V. on behalf of KeAi Communications Co. Ltd.
This is an open access article under the CC BY-NC-ND License (http://creativecommons.org/licenses/by-nc-nd/4.0/).

hydrate-bearing sediment (HBS) properties is fundamental to resource assessment, extraction optimization, and commercial development. Unlike indirect methods such as seismic surveys and wireline logging, *in-situ* pressure-preserved coring directly recovers undisturbed samples for comprehensive laboratory analysis of phase distribution, pore architecture, flow properties, and THMC coupling during production (Wan Y et al., 2022). This first-hand geological evidence provides irreplaceable data for precise reservoir evaluation and efficient NGH development (Dai S et al., 2017; Xu M et al., 2026). NGH reservoirs exist in extreme subsea environments hundreds to thousands of meters below the seafloor, where thermodynamic stability is critically sensitive to temperature-pressure perturbations. Minor environmental disturbances during coring can trigger rapid dissociation, causing pore restructuring, permeability alterations, and mechanical property degradation that compromise sample integrity and reliability.

Over four decades, pressure-preserved coring technologies for major NGH exploration campaigns have evolved through interdisciplinary contributions from marine geology, petroleum engineering, oceanography, and geotechnical communities. Scientific ocean drilling programs pioneered early developments with the Pressure Core Barrel (DSDP Leg 76, 1980) (Rabinowitz PD et al., 1985), followed by the improved Pressure Core Sampler (ODP) (Kvenvolden KA and Cameron D, 1983; Dickens GR et al., 2000), FUGRO Pressure Corer and HYACE Rotary Corer (IODP) (Amann H et al., 1997; Schultheiss P et al., 2009), Pressure Temperature Core Sampler and Hybrid PCS (Nankai Trough) (Wakishima R, 1998; Kubo Y et al., 2014), Pressure Corer Tools with Ball Valves (NGHP and Gulf of Mexico) (Schultheiss P et al., 2017), and pressure-preserved systems for China's Guangzhou Marine Geological Survey expeditions (GMGS) (Lu QP et al., 2024). These collaborative efforts across research consortiums, national laboratories, and international collaborations have enabled successful core recovery under near *in-situ* conditions through mechanical valve sealing and accumulator pressure regulation.

Current NGH coring employs pressure compensation systems with thermal insulation barriers, using mechanical valves and accumulators for pressure maintenance while relying on aerogel insulation for thermal protection. Despite excellent pressure control, significant temperature management deficiencies persist: During drilling completion and core retrieval, decreasing water depth and rising environmental temperature create drastic thermodynamic boundary changes. Real-time monitoring from Japan's 2012–2013 Nankai Trough expedition revealed that even under pressure preservation, core temperature-pressure states deviated from hydrate phase equilibrium, triggering irreversible dissociation (Collett TS et al., 2015; Inada N and Yamamoto K, 2015). The ODP Leg 204 pressure explosion caused by massive in-core hydrate dissociation and methane release demonstrated severe safety risks while highlighting complete sample loss potential (Bohrmann G et al., 2002).

Multi-field coupling approaches for hydrate reservoir simulation have evolved significantly over recent decades. Traditional thermal-hydraulic-mechanical (THM) models initially addressed basic coupling mechanisms, subsequently expanding to thermal-hydraulic-mechanical-chemical (THMC) frameworks that incorporate hydrate dissociation kinetics and chemical reactions. Recently, Li YL et al. (2024) proposed the thermal-hydraulic-mechanical-chemical-sand (THMCS) coupling framework that extends THMC models by explicitly incorporating solid particle transport as an independent field, addressing sand production challenges during long-term hydrate exploitation. This five-field coupling approach represents an important advancement for production-scale reservoir analysis where sand migration becomes critical for wellbore stability and production optimization.

Using actual NGH cores from China's GMGS expeditions in the Shenhu area, South China Sea, this study systematically investigates temperature-pressure synergistic control mechanisms and spatiotemporal evolution patterns in NGH core property changes through integrated theoretical analysis, numerical simulation, and experimental validation, establishing foundations for scientifically based temperature-pressure preservation technology (Wan Y et al., 2022). This study develops fully coupled THMC numerical models incorporating hydrate dissociation kinetics, multiphase fluid migration, heat/mass transfer, and mechanical deformation, validated against geological data from China's GMGS expeditions in the Shenhu area, South China Sea. Through systematic multi-physics field response analysis under varying environmental temperatures, the authors reveal temperature control mechanisms governing hydrate dissociation behavior during core retrieval processes. These findings provide scientific guidance for optimizing NGH preservation technologies.

2. *In-situ* physical property characterization of NGH core

2.1. Core sample acquisition and reservoir properties

Shenhu area, located on the northern continental slope of the South China Sea east, represents a key NGH exploration target in Chinese waters. This region exhibits highly heterogeneous hydrate saturation distribution (Qin XW et al., 2020, 2022). Integrated numerical modeling and wireline logging indicate saturations 10%–40%, with enriched zones exceeding 40%. Hydrates occur primarily in cementing mode, closely bonded with sediment particles (Zhang RW et al., 2018). The GMGS-1 expedition in 2007, led by Guangzhou Marine Geological Survey, conducted pressure-preserved coring using FUGRO Pressure Corer and FUGRO Rotary Pressure Corer (Wang JG et al., 2014). Five sites were sampled (SH1, SH2, SH3, SH5, SH7), with physical hydrate recovery at sites SH2, SH3, and SH7. SH2, drilled to 260

mbsf along the western ridge, confirmed NGH occurrence in a 25 m interval above the base of gas hydrate stability zone (BGHSZ). Pore water freshening analysis revealed average hydrate saturations of 25%–46%, uniformly dispersed within unconsolidated fine-grained clay and sandy clay (Kuang YW et al., 2019).

To investigate THMC coupling characteristics during NGH dissociation, the authors selected pressure-preserved cores from Shenhu sites SH2 and SH3 (SH2-12R, SH3-7P, SH3-13P) as research subjects. Physicochemical parameters were obtained through complementary techniques: (1) Pressure-preserved coring for *in-situ* sample recovery; (2) wireline data inversion for continuous formation profiling; (3) pore water chemistry for saturation distribution; (4) controlled gas release experiments for compositional analysis (Li CH et al., 2014; Wang JG et al., 2014). Core macroscopic characteristics show gray to dark gray muddy silt with dense microstructure dominated by micropores (<2 μm) and mesopores (2–10 μm). Acoustic and resistivity logs exhibit distinct positive anomalies, combined with methane-dominated (>99%) gas composition confirmed by chromatographic analysis, collectively indicating high-saturation NGH enrichment at these intervals (Lu C et al., 2022).

2.2. Multi-physics coupling simulation parameter determination

Based on comprehensive multi-source data analysis, Table 1 establishes the parameter system for THMC coupled numerical simulation. This encompasses key physical properties required for multi-physics coupling analysis. Parameter values prioritize measured data from site SH2, with reasonable supplementation from similar international hydrate reservoirs for difficult-to-measure parameters, ensuring model reliability.

NGH core permeability exhibits enormous variability depending on hydrate morphology (Ji YK et al., 2022). Selecting appropriate permeability evolution models is crucial for accurately predicting fluid migration during dissociation. This study adopts the dynamic permeability model by Liang W et al. (2022), which considers composite pore morphology, capillary roughness, and elastic damage from hydrate dissociation (Wang JG and Peng Y, 2014). Relative permeability is expressed as (Eq. 1):

$$k_{rh} = k_0 \left(1 - \frac{S_{hc} + \sqrt{S_{hf}}}{1 - C_{h,\lambda}} \right)^4 \tag{1}$$

where S_{hc} and S_{hf} are the saturations of grain-coating and pore-filling hydrate, respectively, $C_{h,\lambda}$ is the initial roughness, k_0 is initial permeability. Porosity and dynamic absolute permeability of NGH cores are expressed as respectively (Eqs. 2, 3):

$$\phi = \left(\frac{1}{1+\varepsilon_v} \right) (\phi_0 + \varepsilon_v + (1-\phi_0)(P - P_0)/K_s) \tag{2}$$

$$k = k_0 \left(1 - \frac{S_{hc} + \sqrt{S_{hf}}}{1 - C_{h,\lambda}} \right)^4 \left(\frac{\phi}{\phi_0} \right)^3 \tag{3}$$

where ϕ_0 is the initial porosity, P and P_0 are pore pressure and initial pore pressure, ε_v (Eq. 4) and ε_{v0} are the volumetric strains at any given time and initial time, respectively.

$$\varepsilon_v = \nabla \cdot \boldsymbol{u} \tag{4}$$

where $\boldsymbol{u}$ is displacement vector.

To enhance model physical realism and predictive capability, the authors employ parameter calibration based on NMR-measured permeability and hydrate saturation data from GMGS-1 Shenhu cores by Li CH et al. (2014). Nonlinear least-squares fitting of measured data reflects permeability evolution under changing pore structure, yielding $C_{h,\lambda} = 0.4096$, $S_{hc}/S_h = 0.999$, $S_{hf}/S_h = 0.001$. Fig. 1 demonstrates that within hydrate saturation range of 0–0.5, model predictions agree well with the relative permeability measurements ($R^2 = 0.9572$, RMSE = 0.0667, MAE = 0.0472)

Table 1. *In-situ* physical parameters for multi-physics field coupling numerical simulation.

Parameter Name	Value	Unit	References
Initial porosity (ϕ_0) *	0.25	\	(Li CH et al., 2014; Wang XJ et al., 2014; Zhang RW et al., 2018; Li J et al., 2019; Kuang YM et al., 2019; Lu C et al., 2022; Li YL et al., 2024; Wang H et al., 2024)
Initial hydrate saturation (S_{h0}) *	0.40	\	
Initial water saturation (S_{w0})	0.35	\	
Initial gas saturation (S_{g0})	0.25	\	
Initial permeability (k_0) *	98	mD	
In-situ pressure (P_{g0}) *	10	MPa	
In-situ temperature (T_0) *	283.15	K	
Sediment density (ρ_s) *	1250	kg/m^3	
Gas hydrate density (ρ_h) *	913	kg/m^3	
Water density (ρ_w) *	1054	kg/m^3	
Sediment elastic modulus (E) *	460	MPa	
Sediment particle bulk modulus (K_s)	15	GPa	
Poisson's ratio (ν) *	0.15	\	

Note: * indicates that the data come from actual measurements at SH2 and SH7 sites.

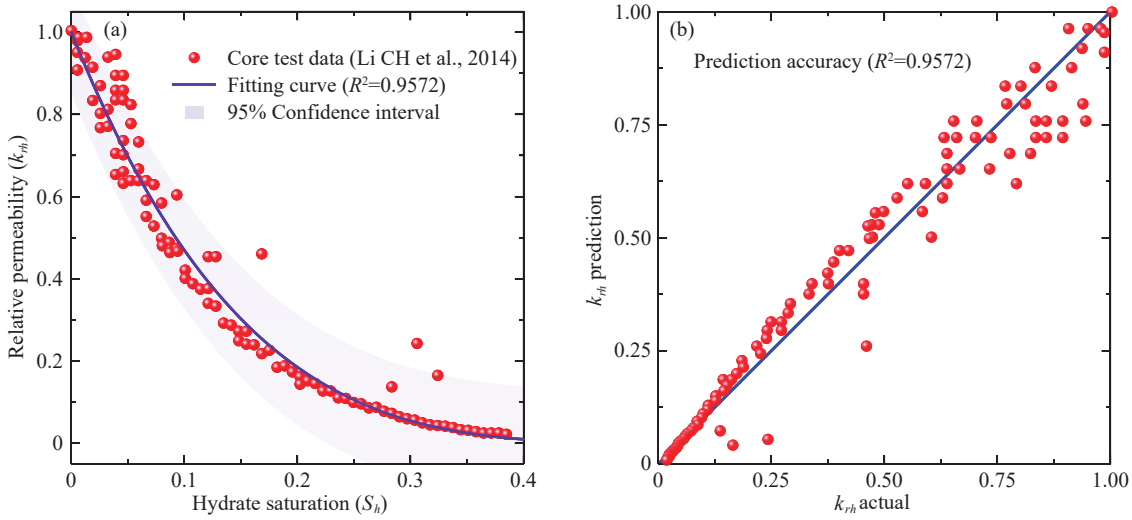

Fig. 1. a–Fitting plot of dynamic permeability model based on measured data (after Li CH et al., 2014); b–prediction accuracy plot of dynamic permeability model fitting.

(Li CH et al., 2014). The model effectively captures permeability decline trends in medium-to-high saturation ranges, demonstrating good adaptability for composite morphology hydrate reservoirs and providing reliable permeability evolution description for THMC coupling simulation.

3. Fully coupled THMC multi-physics model for NGH core

For hydrate-bearing sediments, the thermal-hydraulic-mechanical-chemical (THMC) coupling process involves four key physical fields: Chemical reactions governing NGH dissociation, two-phase fluid flow in porous media, heat transfer with phase change effects, and mechanical deformation under varying pore pressure conditions.

3.1. Basic assumptions for multi-physics coupling model

Hydrate dissociation in porous media involves complex coupling of fluid flow, heat transfer, deformation, and phase transitions. To establish a mathematically tractable model reflecting primary physical mechanisms, the authors propose the following assumptions for simulating NGH dissociation in cores.

(i) Since gas release tests confirm >99% methane content; cores contain pure methane hydrate (Type I structure) with formula $CH_4 \cdot N_hH_2O$.

(ii) NGH exists as solid phase within pores or adhered to sediment particles, consistent with the permeability model composite morphology description.

(iii) Given short-term coring characteristics, secondary hydrate formation from local cooling or pressure fluctuations during dissociation is neglected.

(iv) Both water and gas two-phase flow follow Darcy's law, with each phase having independent permeability and saturation.

(v) Given that the pore scale is much smaller than the macroscopic characteristic scale, sediment skeleton, hydrate, water, and gas maintain thermal equilibrium within representative volume elements.

(vi) Temperature variations during pressure-preserved coring (<20 K) generate from hydrate dissociation.

For hydrate-bearing cores, sediment forms the skeleton with hydrate, water, and gas occupying pore space. Porosity is defined as (Eq. 5):

$$\phi = \frac{V_h + V_w + V_g}{V_s + V_h + V_w + V_g} \tag{5}$$

where V_i $(i = h, w, g)$ represent hydrate, water, and gas volumes, V_s is sediment particle volume, and phase saturations are expressed as (Eq. 6):

$$S_i = \frac{V_i}{V_h + V_w + V_g} (i = h, w, g) \tag{6}$$

During hydrate dissociation, phase saturation sum equals unity: $S_h + S_w + S_g = 1$.

3.2. THMC multi-physics coupling mathematical framework

For hydrate-bearing sediments, when external temperature-pressure conditions reach hydrate thermodynamic equilibrium thresholds, dissociation initiates. The chemical reaction adopts the classical Kim-Bishnoi kinetic model (Kim HC et al., 1987; Hong H et al., 2003).

$$CH_4 \cdot N_hH_2O_{(S)} \xrightarrow{T\uparrow, P\downarrow} CH_{4(g)} + N_hH_2O_{(l)} \tag{7}$$

Where the hydrate dissociation rates can be written as:

$$\rho_h S_h \frac{\partial \phi}{\partial t} + \phi \rho_h \frac{\partial S_h}{\partial t} = -k_{d0} M_h \phi S_h exp(-\Delta E/(RT)) \sqrt{\frac{\phi^3 (1 - S_h)^3}{2k}} (P_{eq} - P_g) \tag{8}$$

where M_h is the molar masses of hydrate, k_{d0} is the chemical reaction kinetic constant, A_s is the specific surface area for dissociation reaction, ΔE is the activation energy, R is the ideal gas constant, T is temperature, P_g is the pore gas pressure, P_{eq} is the critical equilibrium pressure of NGH, and k is the absolute permeability.

According to the assumptions in this study, the hydrate reservoir consists of three phases (solid phase, liquid phase, and gas phase) and four components (sediment particles, NGH, water, and methane gas) (Leverett MC, 1941; Gershenzon NI et al., 2016; Ma TR et al., 2017). The mass conservation equations for the water and gas two-phase components are:

$$\rho_w\left(S_w\frac{\partial\phi}{\partial t}+\phi\frac{\partial S_w}{\partial t}\right)+\nabla\left(\frac{k_{rw}k\rho_w}{\mu_w}\left(P_{e0}\left(-\frac{1}{\lambda}\right)\left((S_e)^{-1/\lambda-1}\right)\nabla S_w+\rho_w\vec{g}-\nabla P_g\right)\right)=N_hM_wk_{d0}\phi S_h exp(-\Delta E/(RT))\sqrt{\frac{\phi^3(1-S_h)^3}{2k}}\left(P_{eq}-P_g\right) \tag{9}$$

$$\frac{M_g}{RT}\left(S_gP_g\frac{\partial\phi}{\partial t}+\phi S_g\frac{\partial P_g}{\partial t}+\phi P_g\frac{\partial S_g}{\partial t}\right)-\frac{M_g\phi S_gP_g}{RT^2}\frac{\partial T}{\partial t}+\nabla\left(\frac{k_{rg}kM_gP_g}{\mu_gRT}\left(\frac{M_gP_g\vec{g}}{RT}-\nabla P_g\right)\right)=M_gk_{d0}\phi S_h exp(-\Delta E/(RT))\sqrt{\frac{\phi^3(1-S_h)^3}{2k}}\left(P_{eq}-P_g\right) \tag{10}$$

where k_{rw} and k_{rg} are the relative permeabilities of water and methane respectively, S_e is the effective water saturation, S_{wr} and S_{gr} are the residual saturations of methane and water respectively, N_h is the hydration number, M_h, M_w and M_g are the molar masses of hydrate, water, and gas respectively.

The hydrate dissociation process involves both heat conduction and heat convection. When hydrate transforms from solid phase to gas and liquid phases (Kamath VA, 1984; Youslf MH et al., 1991), it absorbs heat. Therefore, the energy conservation law during hydrate dissociation is:

$$\underbrace{C_T\frac{\partial T}{\partial t}}_{Heatstorage}+\underbrace{\nabla(-K_T\nabla T)}_{Heatconduction}+\underbrace{\nabla\left(\phi S_gC_g\rho_g\vec{u_g}T+\phi S_wC_w\rho_w\vec{u_w}T\right)}_{Heatconvection}=\underbrace{Q_h}_{Latentheat} \tag{11}$$

where ρ_i, S_i, C_i, $\lambda_i(i=h,w,g)$ are the density, saturation, specific heat capacity, and thermal conductivity of the i−th phase respectively. ρ_s, S_s, C_s, λ_s are the density, saturation, specific heat capacity, and thermal conductivity of the sediment phase, respectively. C_1 and C_2 are fitting coefficients.

The equilibrium differential equation expressed in displacement form considers the effects of pore pressure and temperature changes, and its tensor form is expressed as:

$$G\nabla^2\boldsymbol{u}+\frac{G}{1-2\nu}\nabla(\nabla\boldsymbol{u})-\alpha\nabla P+\vec{f_k}=0 \tag{12}$$

where G is the shear modulus, α is the Biot coefficient, ν is Poisson's ratio, $\vec{f_k}$ and $\boldsymbol{u}$ are the body force and displacement, respectively.

This system of coupled equations describes the complex interactions between chemical dissociation kinetics, multiphase fluid flow, heat transfer, and mechanical deformation in NGH-bearing cores under temperature perturbations. Detailed derivations of the governing equations, constitutive relationships, and parameter definitions are provided in Appendix A.

4. Model setup based on *in-situ* coring practice

4.1. Boundary condition settings

Building upon the sophisticated engineering practices of pressure-preserved coring operations during the GMGS series expeditions in the Shenhu area, South China Sea, this study establishes a comprehensive boundary condition framework that authentically captures the complex physical constraints encountered in actual seafloor operations. Fig. 2 shows the complete engineering workflow. First, polycrystalline diamond compact (PDC) coring systems retrieve hydrate-bearing cores. After sampling, the cores are immediately sealed into dedicated pressure-preserved barrels. Precision accumulator units inside the barrels sustain hydrostatic pressure close to *in-situ* levels. Meanwhile, high-strength barrel walls provide robust radial confinement for the cores.. This engineering design effectively ensures core internal pressure stability while strictly limiting radial expansion deformation of the cores. Considering that modern pressure-preserved corers typically incorporate dedicated axial expansion buffer spaces to accommodate large-volume gas release during hydrate dissociation processes (methane gas volumes can reach 160 times that of the original solid hydrate), thereby preventing excessive axial stress concentration phenomena, this engineering characteristic manifests as axial free boundary conditions in numerical simulation.

To simulate the coring conditions under the above *in-situ* environment, the boundary conditions set in the model preprocessing stage are shown in Table 2: Radial displacement constraint boundary condition at $r=r_{max}$ ($u_r=0$). Axial stress-free boundary conditions at $z=0$ and $z=z_{max}$ ($\sigma_z=0$), the pressure inside the tube is maintained constant at the *in-situ* pressure measured during the coring process through the accumulator regulation system, which is reflected as a constant external pressure boundary condition P_{is} = 10 MPa. As shown in Fig. 3, combining the environmental temperatures recorded in the NGH coring

practices of India's NGHP-01 and Japan's 2012 Nankai Trough (Dai S and Santamarina JC, 2014; Inada N and Yamamoto K, 2015), the environmental temperatures are set to 293.15 K, 298.15 K and 303.15 K, representing the driving forces of different environmental temperatures on the *in-situ* state of the core. To balance computational accuracy and efficiency, the core model established in this study has a radius of 25.5 mm and a length of 300 mm, consistent with standard pressure-preserved core dimensions. The specific geometric configuration and mechanical boundary conditions are shown in Fig. 4.

4.2. Simulation parameter determination

To accurately simulate the THMC coupling behavior

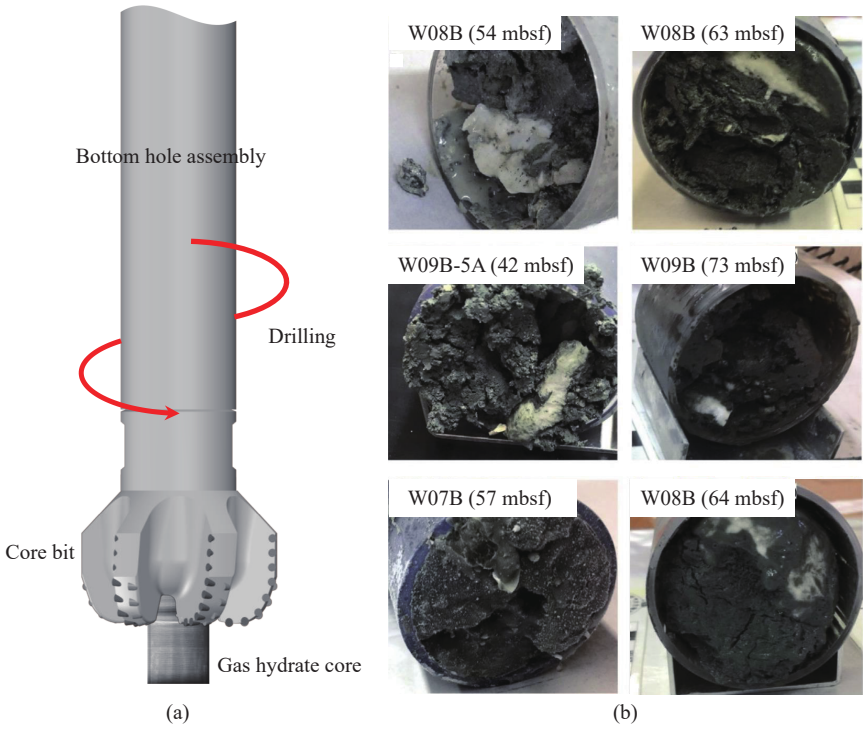

Fig. 2. a–Hydrate reservoir coring methods in the Shenhu area during GMGS series expeditions; b–cross-section of NGH core cutting inside the coring tube during GMGS-5 exploration expedition (after Wei JG et al., 2019; Xu M et al., 2026).

Table 2. Gas hydrate core boundary condition settings.

Boundary expression	$r = 25.5$ mm	$z = 0$ mm	$z = 300$ mm
Boundary conditions	$u_r = 0$	$u_z = 0$	$\sigma_z = 0$
	$\frac{\partial P_g}{\partial r} = 0$	$P = P_{is}$	$P = P_{is}$
	$T = T(t)$		

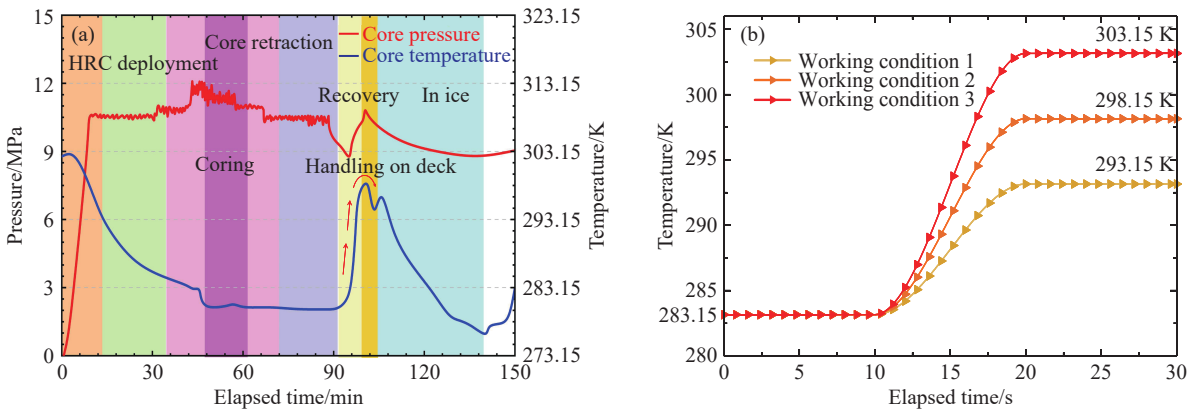

Fig. 3. a–Pressure and temperature distribution recorded during the recovery of core NGHP-1-12A-06E with the HYACE Rotary Corer in the voyage NGHP-01 Expedition (after Wei JG et al., 2019; Xu M et al., 2026); b–temperature boundary condition settings during numerical simulation.

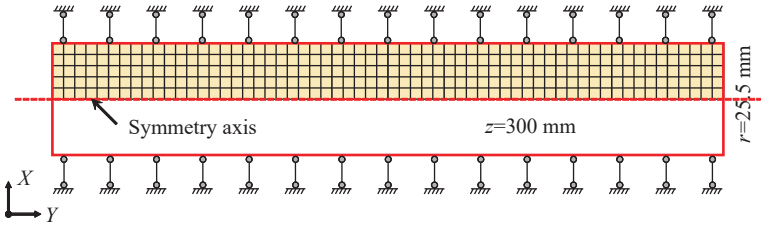

Fig. 4. Core model geometry and mechanical boundary condition settings.

Table 3. Physical property parameters for multi-physics field coupling simulation numerical calculation.

Parameter	Value	Unit	Parameter	Value	Unit
N_h	6	\	S_{wr}	0.10	\
M_h	0.124	kg/mol	S_{gr}	0.05	\
M_w	0.018	kg/mol	c_s	950	J/kg·K
M_g	0.016	kg/mol	c_h	2010	J/kg·K
k_d^0	3.60×10^4	mol/m^2·Pa·s	c_w	4200	J/kg·K
ΔE	81084.20	J/mol	c_g	2180	J/kg·K
R	8.314	J/mol·K	λ_s	1.2	W/m·K
e_1	44.36	\	λ_h	2.0	W/m·K
e_2	8068.02	K	λ_w	0.50	W/m·K
μ_w	1.01×10^{-3}	Pa·s	λ_g	0.06	W/m·K
μ_g	1.84×10^{-5}	Pa·s	C_1	56599	J/mol
m	0.6	\	C_2	16.744	J/mol·K
P_{e0}	0.1	MPa	α	0.4	\
λ	2	\	$\vec{g}$	9.81	m/s^2

during NGH coring in the Shenhu area of the South China Sea, this study systematically collected and determined the key physical property parameters required for numerical calculations as shown in Table 3. The parameters prioritize *in-situ* test data from the GMGS series expeditions to ensure the reliability of model inputs, supplemented by relevant literature data, covering multiple physical processes including hydrate dissociation kinetics, multiphase fluid properties, heat transfer characteristics, and soil mechanics. Among these, the hydrate chemical parameters adopt standard values from the classical Kim-Bishnoi dissociation model (Kim HC et al., 1987; Zhang LM et al., 2019). Thermal property parameters (specific heat capacity and thermal conductivity) for each phase are adopted from hydrate characteristic datasets reported by Sloan ED and Koh CA (2008) and Zhang Y et al. (2022), whereas the thermal properties of the sediment skeleton use measured silty clay data from the Shenhu area (Wang JG et al., 2014). Fluid property parameters such as viscosity and density of water and methane adopt experimental values under standard temperature and pressure conditions (Wu NY et al., 2010; Liu CL et al., 2012). Soil mechanical parameters, particularly the elastic modulus and Poisson's ratio of sediments, directly adopt triaxial compression test results of fine-grained sediments in the Shenhu area (Wei JG et al., 2021).

4.3. Numerical methods for coupled model

This study employs COMSOL Multiphysics software to solve the thermal-hydraulic-mechanical-chemical (THMC) coupled processes of NGH cores simultaneously within a unified framework. The COMSOL solver utilizes the pre-configured COMSOL Geomechanics module for the geomechanically part, while domain ordinary differential and differential-algebraic equations are used to solve the NGH dissociation field of the core. Two-phase fluid flow and core heat transfer employ the general form partial differential equation module to avoid convergence difficulties when using traditional separate solution methods for different physical processes.

The numerical model addresses four key physical fields: NGH dissociation kinetics with NGH saturation as the solving variable, two-phase fluid flow governed by gas phase pressure and water phase saturation as primary variables, heat transfer field using temperature as the solving variable considering multiphase fluid convective and conductive effects, and mechanical deformation field handling stress-strain relationships in the porous medium. Strong coupling between these physical fields is achieved through state variables including saturation, pressure, temperature, and mechanical deformation, enabling accurate description of complex response behaviors in NGH cores under temperature perturbations and ensuring relatively stable and robust convergence in COMSOL Multiphysics software. Detailed numerical equations and solution algorithms are provided in Appendix B.

4.4. Grid independence and convergence analysis

To ensure numerical solution reliability and accuracy, particularly in regions with steep gradients such as hydrate dissociation fronts, systematic grid independence verification and convergence analysis were conducted. Three mesh configurations were established to evaluate mesh sensitivity: coarse mesh (15420 elements), medium mesh (22850 elements), and fine mesh (428360 elements). Mesh refinement was strategically concentrated in critical regions where steep gradients occur, including the dissociation front zone, with local element sizes ranging from 0.25 mm to 1 mm.

As shown in Table 4, grid independence assessment focused on key variables that drive the THMC coupling processes: Hydrate saturation (S_h), pore pressure (P_g), and temperature (T). Monitoring points were established at critical locations including the core geometric center and the hydrate dissociation front to capture maximum gradient

Table 4. Grid independence and convergence analysis results.

Mesh configuration	Core center			Dissociation front		
	Peak pore pressure/MPa	Temperature/K	Saturation	Peak pore pressure/MPa	Temperature/K	Saturation
Coarse (15420)	10.55	284.8	0.380	10.002	283.5	0.380
Medium (22850)	10.79	285.2	0.384	10.008	283.9	0.384
Fine (428360)	10. 82	285.6	0.385	10.01	284.1	0.384

Note: Grid independence and convergence analysis at a boundary temperature = 303.15 K. All physical quantities evaluated at t = 300 s.

variations. The convergence criterion was defined as relative errors below 2% between consecutive mesh refinements for all primary variables.

Convergence analysis demonstrates that the medium mesh achieves grid-independent solutions with acceptable accuracy while maintaining computational efficiency. Quantitative results show that relative errors between medium and fine mesh configurations remain below the established convergence criteria: Maximum pressure deviation < 1.8%, temperature variation < 0.5 K, and hydrate saturation difference < 1.5%. These metrics confirm that the medium mesh resolution provides adequate accuracy for capturing steep gradient phenomena in hydrate dissociation fronts.

The convergence analysis validates that the chosen medium mesh configuration (22850 elements) provides reliable numerical solutions while reducing computational cost by 65% compared to the fine mesh. This mesh density ensures accurate representation of THMC coupling mechanisms in hydrate-bearing sediments, particularly in regions where rapid phase transitions and steep property gradients occur during temperature-induced dissociation processes.

5. Coupled results of hydrate dissociation under temperature-driven

Building upon the comprehensive numerical framework, this chapter systematically investigates the multi-physics coupling response characteristics of NGH cores under temperature-driven conditions, and elucidates fundamental mechanisms controlling hydrate stability degradation and resulting impacts on core structural integrity. The investigation encompasses four critical aspects: Temperature and pressure field evolution dynamics, hydrate dissociation kinetics and phase transition processes, mechanical response characteristics under unconfined conditions, and multiphase fluid migration patterns. These findings provide essential insights into the complex feedback mechanisms between thermal disturbances and hydrate core stability, offering crucial guidance for optimizing pressure-preserved coring protocols.

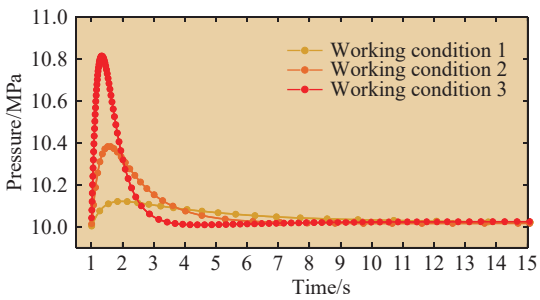

Fig. 5. Temporal evolution curves of pore pressure at the geometric center of the core under different boundary temperature conditions.

5.1. Evolution characteristics of temperature and pressure fields

The pressure field evolution manifests distinctive stepwise response characteristics to thermal boundary conditions, exhibiting consistent pressure disturbance propagation patterns across temperature scenarios while demonstrating significant amplitude variations. Fig. 5 shows the temporal evolution curves of pore pressure at the geometric center of the core under three different boundary temperature conditions: Under 293.15 K conditions, internal pressure fluctuations remain relatively subdued, generating local overpressure of approximately 0.11 MPa with pressure equilibration achieved within 10 s. At 298.15 K, enhanced hydrate dissociation elevates local overpressure to 0.38 MPa, compressing equilibration time to 7 s. Under extreme 303.15 K conditions, intensive hydrate decomposition triggers pressure surges reaching 0.82 MPa, with explosive pressure propagation characteristics and equilibration compressed to 4 s.

Gas compressibility effects amplify pressure pulses when methane accumulation exceeds critical saturation (S_g > 0.3). Real gas behavior under confined conditions contributes 25%–40% of total surge magnitude. Permeability threshold transitions occur when hydrate saturation drops below S_g < 0.2. These transitions trigger explosive permeability increases exceeding three orders of magnitude (about 1 mD to >1000 mD). The sudden permeability changes enable rapid gas mobilization. The temperature-pressure coupling intensity scales exponentially with boundary temperature. This scaling establishes positive feedback mechanisms that accelerate gas hydrate structural degradation. Pressure surges exceeding 0.5 MPa occur within 5–10 s when boundary temperature exceeds 298 K. These rapid pressure changes pose significant risks for pressure-preserved coring operations. The pressure buildup rates exceed 0.1 MPa/s and can overwhelm conventional pressure relief systems. Safe operation requires temperature exposure limits below 295 K and pressure monitoring systems with response time under 3 s.

The boundary configuration permits gas-water exchange at both end faces, generating the spatial pressure distribution

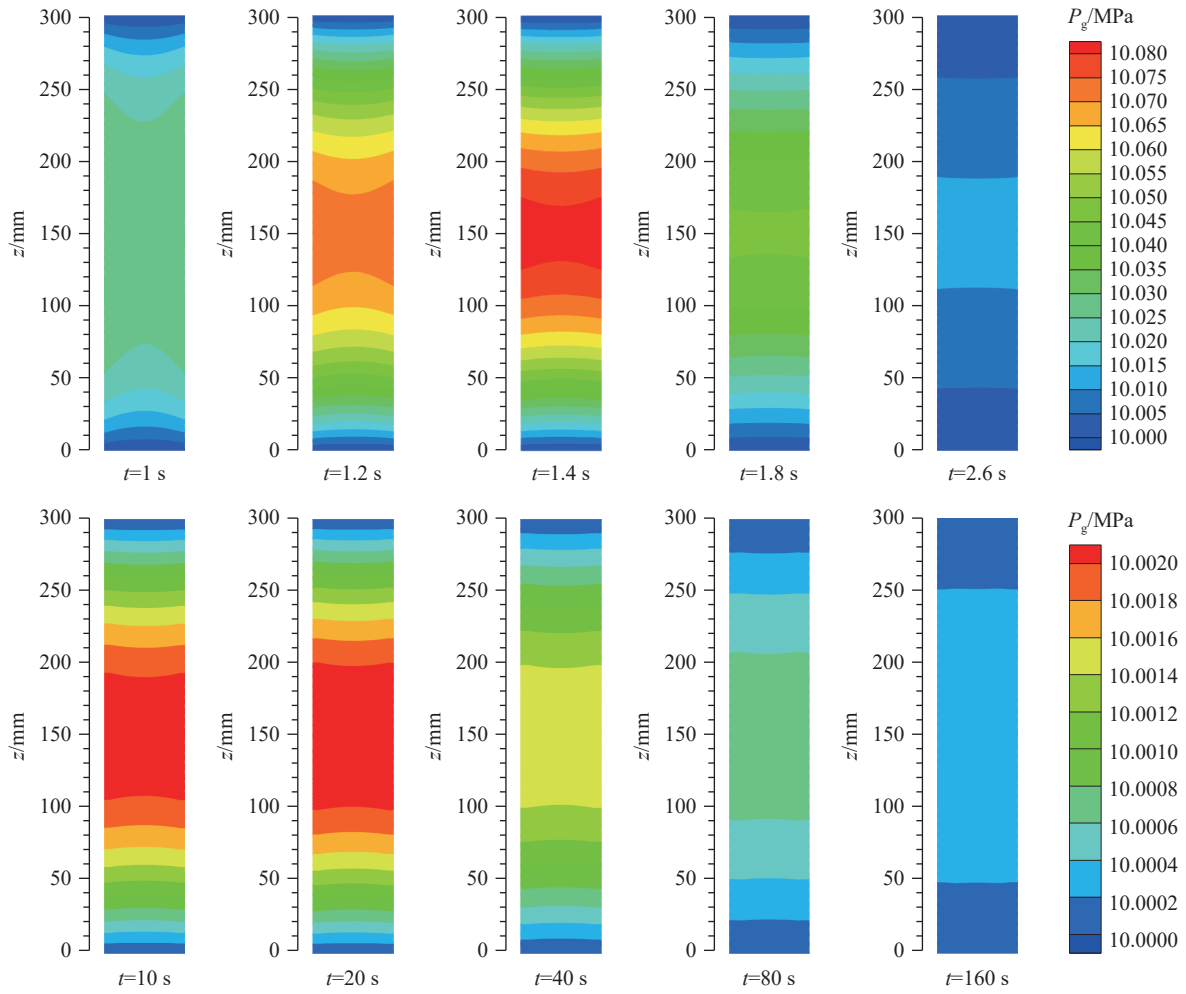

Fig. 6. Pore pressure field perturbation in the core during the initial stage of natural gas hydrate dissociation at boundary temperature of 303.15 K.

depicted in Fig. 6. Pressure disturbances originate from the core center (the primary hydrate dissociation zone) and propagate symmetrically toward both ends with attenuation. Differential boundary constraints at core termini create pronounced central pressure concentration, with end-zone pressure amplification ($z/L \leqslant 0.1$ and $z/L \geqslant 0.9$) diminished by 1.1%–8.2% relative to the central region, forming parallel-advancing pressure fronts. As NGH saturation diminishes, axial pressure gradients exhibit progressively diminishing trends throughout the dissociation process.

Numerical simulation results indicate that the radial temperature distribution exhibits a typical inward diffusion pattern, with temperature gradients decreasing from the core surface toward the center, forming concentric isothermal line distributions. Under 293.15 K boundary conditions, during the initial stage (t < 200 s), the surface temperature rapidly responds to 290–291 K while the center temperature remains at the original *in-situ* temperature of 283.15 K, with radial temperature gradients reaching 8–12 K/cm. During the intermediate stage (200–1000 s), the temperature front advances inward, forming a transitional temperature zone of 285–287 K at the r/R=0.6 position. In the later stage (t > 1000 s), as the overall NGH saturation decreases to relatively low levels, the temperature distribution exhibits typical inward heat conduction patterns. When boundary temperatures increase to 298.15 K and 303.15 K, the radial temperature gradients during hydrate dissociation become significantly steeper, reaching 15–20 K/cm and 25–35 K/cm respectively, with correspondingly increased temperature propagation depths. Under 303.15 K conditions, the high-temperature region (T > 295 K) can extend to the r/R = 0.4 range.

The axial temperature distribution is jointly controlled by end heat dissipation effects and endothermic reactions from hydrate dissociation. The core ends ($z/L \leqslant 0.1$ and $z/L \geqslant 0.9$), due to large exposed surface areas and favorable heat dissipation conditions, exhibit temperature rise rates 20%–30% faster than the central region, creating a “thermal end effect”. The central region ($0.2 \leqslant z/L \leqslant 0.8$) displays relatively uniform temperature distribution, where high hydrate saturation significantly reduces local temperature rise rates through endothermic dissociation reactions, forming temperature “cold spot” phenomena. The temporal evolution process can be divided into three typical stages: Rapid response stage (0–180 s), where surface temperature rises sharply while internal temperature remains essentially unchanged; penetration-diffusion stage (180–900 s), where the temperature front steadily advances inward, forming

distinct temperature gradients; and equilibration stage (after 900 s), where overall temperature gradients tend toward uniformity, but complete thermal equilibration time is prolonged due to the overall influence of hydrate dissociation.

Distinct phase transition regulation effects are observed during temperature propagation. In hydrate dissociation active zones, as shown in Figs. 7, 8, due to the absorption of dissociation latent heat, local temperature rise rates are significantly reduced, forming characteristic "temperature plateau" phenomena. This phenomenon persists for approximately 2000 s under 293.15 K ambient temperature conditions, while shortening to 200–300 s under 303.15 K conditions, indicating that higher ambient temperatures can more rapidly overcome phase transition retardation effects. Upon completion of NGH dissociation, the core center temperature exhibits an accelerated heat transfer trend until approaching the applied boundary temperature. The axial temperature distribution presents relatively uniform characteristics, primarily attributed to the axial boundary conditions set in the model. However, in the core end regions (z < 30 mm and z > 270 mm), due to boundary effect influences, temperature rise rates are 5% higher than those in the central region. Temperature field analysis at the 1000 s moment indicates that under 298.15 K ambient conditions, the core average temperature reaches 285.2 K, which is 4.7 K higher than under 293.15 K conditions. This temperature difference directly drives subsequent multi-physics field response variations.

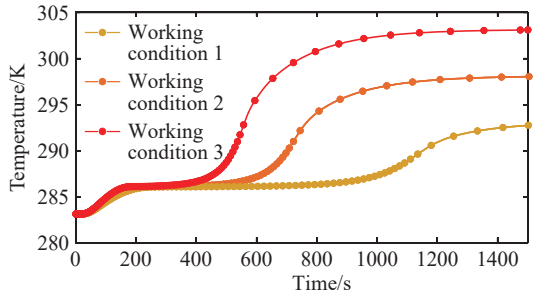

Fig. 7. Temporal evolution curves of temperature at the geometric center of core under different boundary temperature conditions.

5.2. Hydrate dissociation kinetics process

Based on monitoring data from the core geometric center position shown in Fig. 9, the hydrate dissociation process exhibits typical "S-shaped decay" kinetic patterns. The hydrate saturation evolution curves display distinct temperature dependency: Under 293.15 K conditions, hydrate saturation slowly decreases from an initial value of 0.4, with the dissociation process requiring approximately 1200 s for basic completion, whereas under 303.15 K conditions, the dissociation process significantly accelerates, requiring only about 600 s for completion, representing approximately a 2-fold increase in dissociation rate. This temperature sensitivity reflects the Arrhenius characteristics of hydrate dissociation kinetics, where exponential reaction rate growth under high-temperature conditions directly shortens the dissociation time window.

Notably, dissociation curves under all temperature conditions exhibit three-stage characteristics of "slow initiation-rapid dissociation-gradual completion": The initial stage (0–200 s) represents a heat conduction-controlled preheating period with relatively slow dissociation rates; the

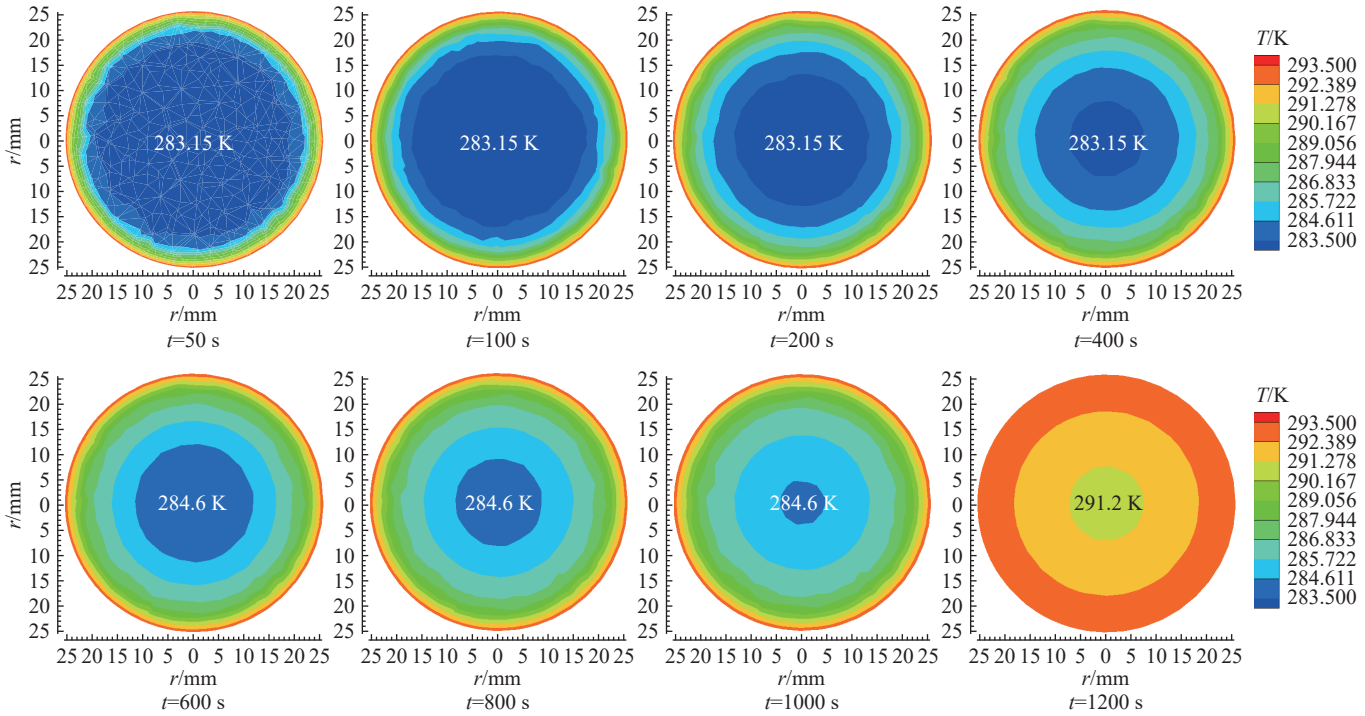

Fig. 8. Temperature gradient in core cross-section during natural gas hydrate dissociation at boundary temperature of 293.15 K.

intermediate stage is the dissociation-dominated period with rapid saturation decline; and the later stage shows gradually decreasing dissociation rates until complete dissociation. As a consequence of hydrate dissociation, pore connectivity undergoes significant changes, with fluid transport capacity remaining severely limited until hydrate saturation decreases below approximately 0.15–0.2, after which continuous pore networks form to facilitate mass transport.

Significantly influenced by temperature spatial distribution characteristics, the equilibrium pressure of NGHs (Fig. 10) exhibits distinct radial stratified distribution characteristics, while the axial distribution tends to be uniform throughout the entire dissociation process. The spatiotemporal distribution evolution of hydrate saturation presents highly non-uniform characteristics. In the dissociation front region, hydrate saturation gradients are extremely large, dropping sharply from the initial value of 0.4 in undissociated regions to near-zero in completely dissociated regions, with gradient changes completed within a radial distance of 10–15 mm. Numerical results show that when the boundary temperature is 293.15 K, hydrates in the boundary region (r > 20 mm) are essentially completely dissociated within 600 s, while the central region (r < 8 mm) maintains relatively high hydrate saturation (S_h > 0.20) throughout the entire 1000 s simulation time.

Quantitative analysis of dissociation rates reveals that local dissociation rates are closely correlated with temperature and pressure gradients, particularly in the later stages of

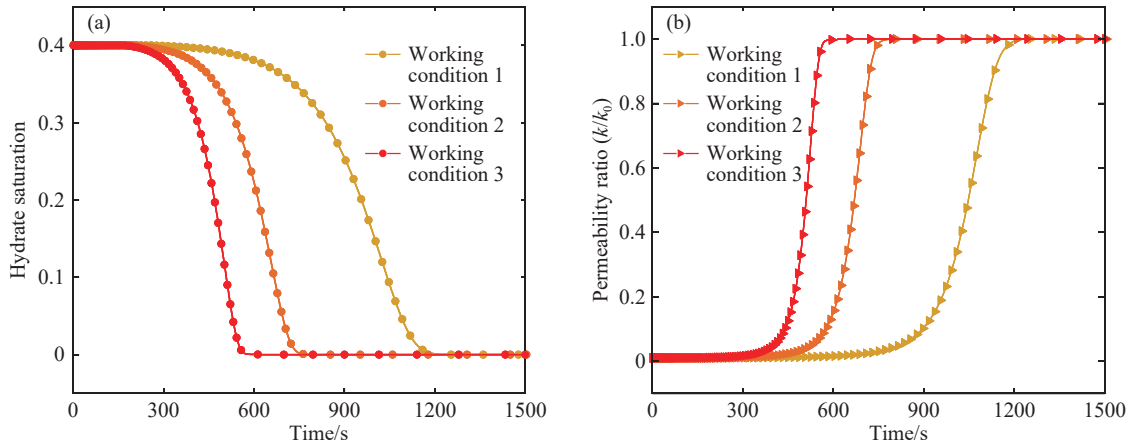

Fig. 9. a–Temporal evolution curves of hydrate saturation at the geometric center of NGH core under different boundary temperature conditions; b–temporal evolution curves of relative permeability at the geometric center of NGH core under different boundary temperature conditions.

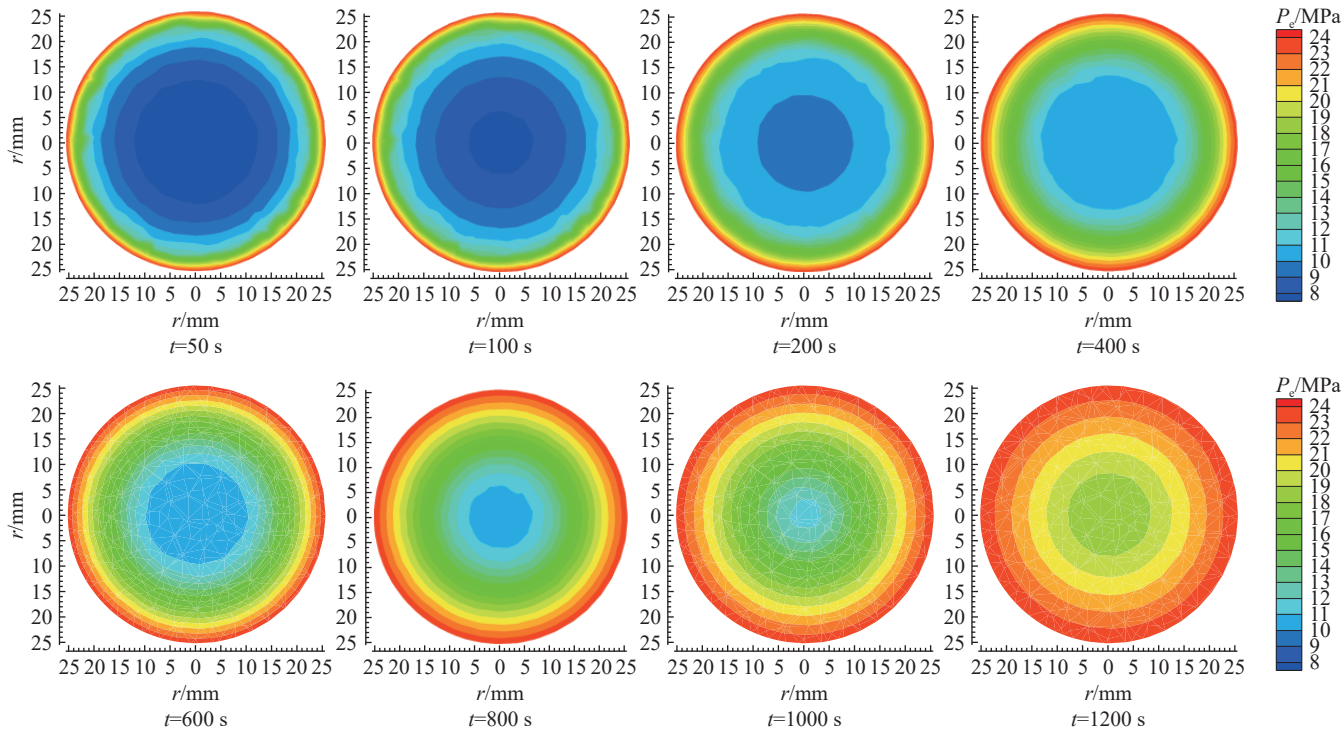

Fig. 10. Equilibrium pressure distribution of NGH in the central cross-section of the core at boundary temperature of 293.15 K.

dissociation when pressure distribution becomes uniform, and the spatial distribution of temperature becomes the determining factor for hydrate dissociation rates. In the most active dissociation regions, instantaneous dissociation rates can reach 250 kg/(m^3·s), which is 2–3 orders of magnitude higher than steady-state dissociation rates. Cumulative dissociation analysis shows that at 1800 s, the overall hydrate dissociation rate in the core reaches 60% under 293.15 K conditions, while dissociation is essentially complete under 303.15 K conditions. A 10 K temperature increase results in approximately 40% improvement in dissociation rate.

5.3. Mechanical response and deformation characteristics

Under experimental conditions without confining pressure constraints, the macroscopic mechanical response of NGH cores exhibits extremely weak characteristics, with overall deformation magnitudes in the range of 10^{-12}–10^{-11} strain, far below the detection precision threshold of conventional rock mechanics testing. Therefore, macroscopic deformation and stress response can be considered negligible in engineering terms. The fundamental reason for this phenomenon lies in the lack of lateral constraint provided by effective confining pressure. Under temperature and pressure disturbances, the core primarily undergoes free expansion or contraction without forming significant stress concentration and strain accumulation. This is in stark contrast to large-scale formation subsidence and wellbore instability caused by hydrate dissociation under *in-situ* formation conditions. The absence of confining pressure eliminates the constraining effect of external stress fields on the core skeleton, significantly weakening the mechanical response during thermo-hydro chemical coupling processes.

Porosity evolution becomes the most important structural parameter change under unconfined conditions, with its change mechanism primarily controlled by pore pressure fluctuations rather than volumetric strain in the traditional sense. The increase in pore pressure acts directly on pore walls, generating outward expansion forces. As shown in Fig. 11, when pore pressure increases from *in-situ* 10 MPa to 10.82 MPa, the pore volume undergoes corresponding minute changes, with porosity increasing from an initial 0.25 to 0.25045. This porosity growth pattern essentially belongs to pressure-driven pore expansion, distinct from volumetric expansion caused by effective stress reduction in conventional consolidation theory. The physical mechanism involves high-pressure gas released from hydrate dissociation directly drives outward deformation of pore walls, causing elastic expansion of the pore network under internal pressure, accompanied by the opening and connection of partial microfractures.

Fig. 12 demonstrates the spatiotemporal evolution process of axial stress in the core under 303.15 K boundary conditions, validating the weak characteristics of mechanical response in hydrate cores under unconfined conditions. The stress distribution exhibits distinct radial symmetry and time dependence: In the initial stage (t = 1.4–3 s), pressure disturbances caused by intense hydrate dissociation lead to stress concentration in the central region, with maximum compressive stress reaching 0.075 MPa; as time progresses, the stress amplitude rapidly decays to approximately 0.09 MPa and tends toward uniform distribution, with the entire evolution process essentially completed within 160 s. The stress magnitude consistently remains within the 0.01–0.1 MPa range, far below the stress levels of conventional rock mechanics testing.

The numerical results further confirm the unique mechanism of core mechanical response under unconfined conditions: The rapid stress decay and spatial homogenization process reflects a free expansion deformation mode rather than the stress accumulation process in traditional consolidation theory. This weak mechanical response makes porosity evolution the most important structural parameter change, with its change mechanism primarily controlled by pore pressure fluctuations rather than volumetric strain, providing a mechanical basis for understanding core structural stability during pressure-preserved coring processes.

5.4. Multiphase fluid migration characteristics

Based on THMC coupled numerical simulation results, the multiphase fluid migration characteristics of NGH cores under different boundary temperature conditions exhibit significant nonlinear evolution patterns and spatial heterogeneous distribution modes. As shown in Fig. 13, under 293.15 K boundary conditions, fluid migration manifests as a relatively slow seepage diffusion process. The spatial distribution characteristics of fluid migration are closely related to the advancement pattern of the hydrate dissociation front, presenting distinct zonal migration phenomena. Gas phase migration velocity ranges from 0 m/s to 0.4×10^{-3} m/s, while water phase migration is relatively lagged with velocities around 0–0.33×10^{-3} m/s.

When the boundary temperature increases to 298.15 K, multiphase fluid migration enters a rapid response stage. The accelerated hydrate dissociation rate triggers substantial methane gas release, causing pore pressure surges. Gas phase migration velocity rises to 0.66×10^{-3} m/s and water phase migration velocity increases to 0.53×10^{-3} m/s. A significant characteristic of this stage is the formation of distinct “viscous fingering” phenomena, where high-pressure methane gas rapidly advances along preferential flow channels.

Under extreme high-temperature conditions of 303.15 K, multiphase fluid migration exhibits explosive characteristics. Large-scale hydrate dissociation triggers chain reactions, with gas phase migration velocity reaching 1×10^{-3} m/s and water phase migration velocity increasing to 1.25×10^{-3} m/s. The most significant phenomenon under these conditions is the spatial differentiation of multiphase fluid migration, where

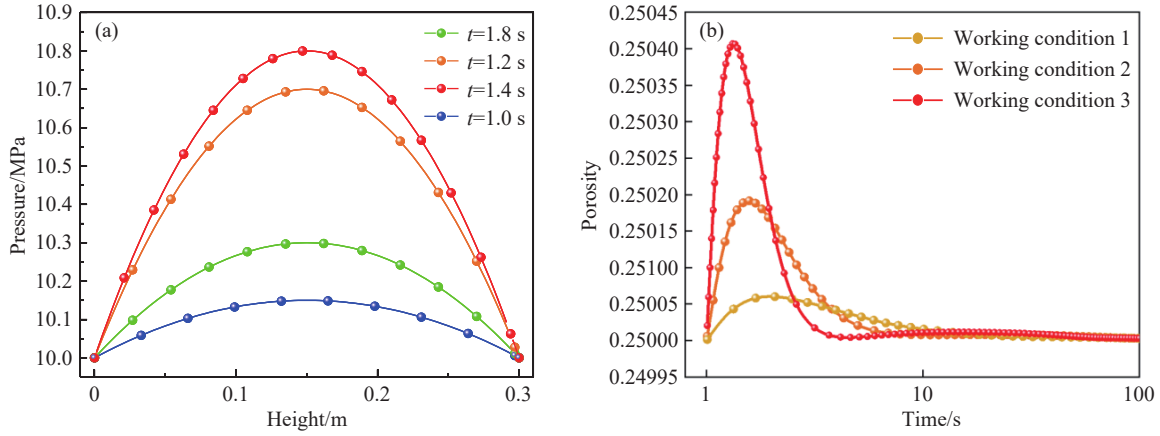

Fig. 11. a–Axial distribution of pore pressure along the core at boundary temperature of 303.15 K; b–temporal evolution curves of porosity at the geometric center of the core under different boundary temperature conditions.

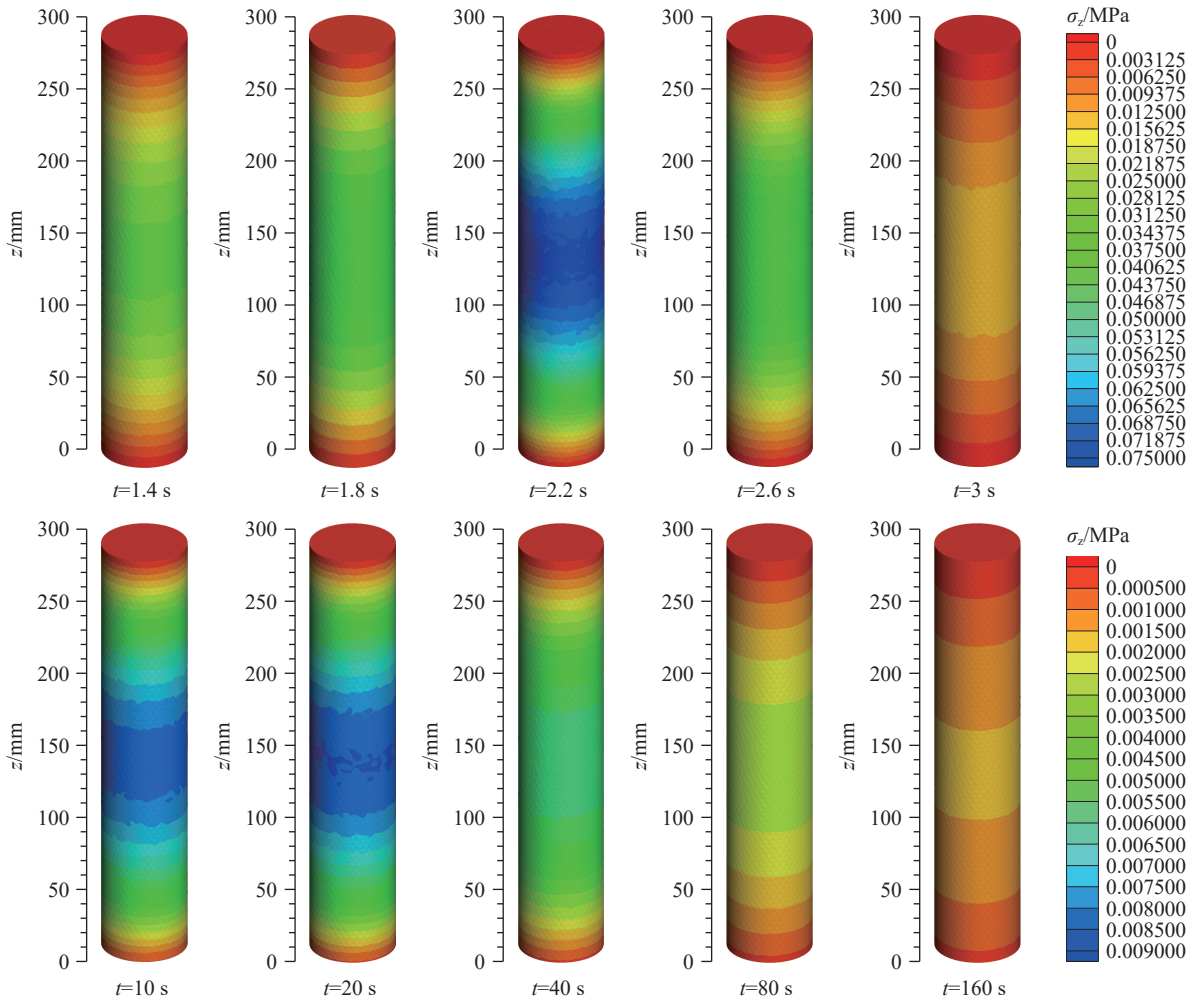

Fig. 12. Spatiotemporal evolution distribution of axial stress in the core at boundary temperature of 303.15 K.

gas phase fluids primarily diffuse radially outward, forming a radial migration pattern with the core center as the source point.

The interphase interaction mechanisms during multiphase fluid migration exhibit strong temperature dependence. Under low-temperature conditions, water-gas two-phase flow primarily manifests as competitive migration, while under high-temperature conditions, gas phase pressure gradients become the dominant controlling factor. Capillary effects are diluted, and gas-water two-phase migration presents quasi-independent parallel flow characteristics.

Like the depressurization measurements conducted by Guo XY et al. (2023) for NGH dissociation processes, the gas production during NGH dissociation caused by rising

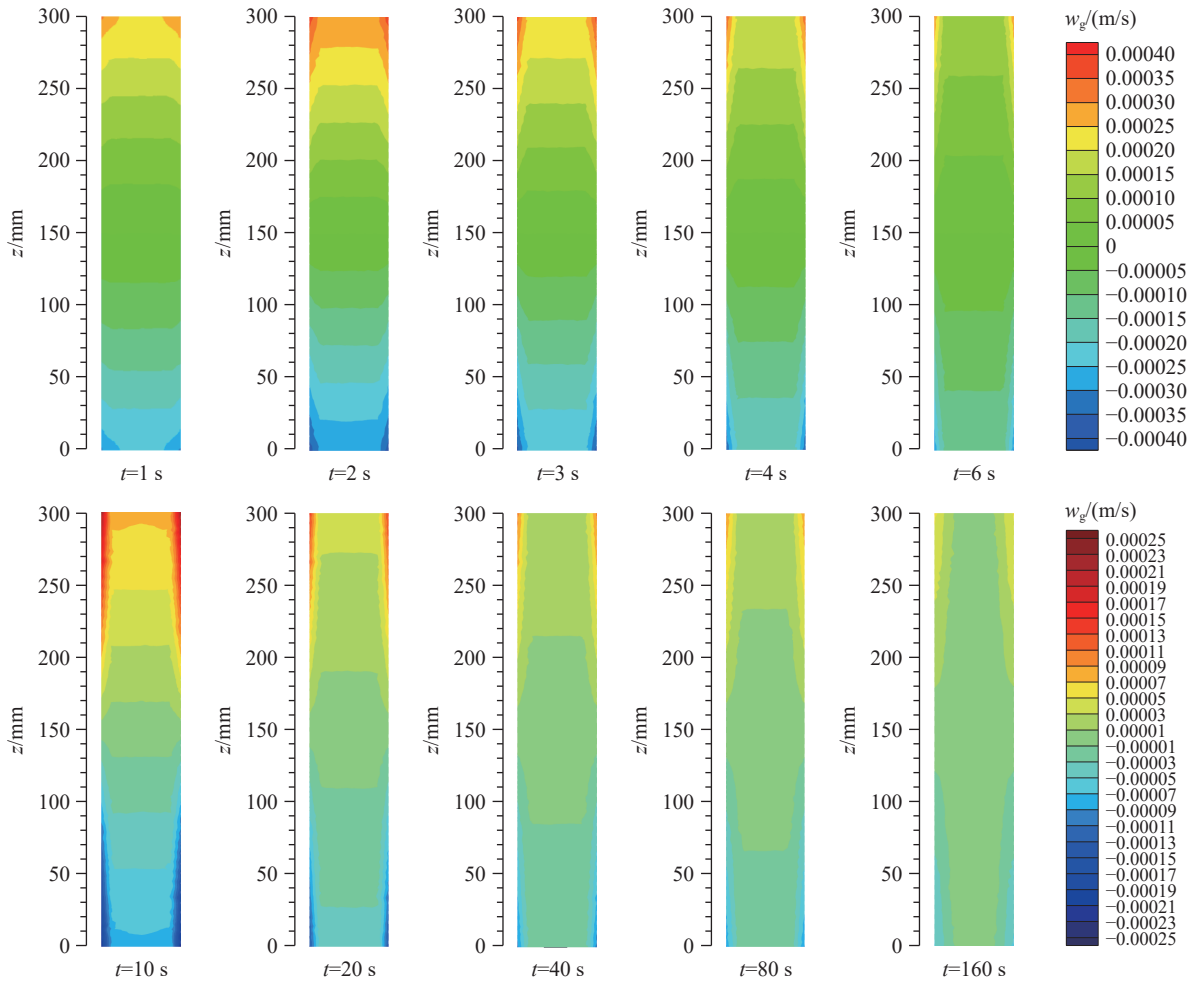

Fig. 13. Spatial distribution of gas migration velocity within the core at boundary temperature of 293.15 K.

environmental temperature also exhibits typical "burst-decay" kinetic characteristics. As shown in Figs. 14, 15, the gas production rate curves present a classic single-peak distribution pattern: In the initial stage (0–5 s), with the rapid propagation of boundary temperature and the disruption of hydrate phase equilibrium conditions, methane production rate rises sharply and reaches its peak within 2–4 s. The peak gas production rate under 303.15 K conditions is approximately 8 times higher than that under 293.15 K conditions, reflecting the exponential influence of temperature on hydrate dissociation kinetics. After reaching the peak, the gas production rate exhibits exponential decay. This decay process is closely related to the reduction in hydrate saturation, the decrease in effective dissociation area, and the increase in mass transfer resistance.

5.5. Comprehensive parameter comparison and temperature sensitivity analysis

The comprehensive parameter analysis in Table 5 reveals fundamental scaling laws governing THMC coupling processes. Three distinct temperature sensitivity regimes emerge: Pressure-related parameters exhibit exponential amplification, temporal parameters follow power-law acceleration, while saturation parameters demonstrate logarithmic growth. This hierarchy of temperature sensitivity indicates that pressure management, rather than dissociation kinetics or gas production, becomes the critical limiting factor in elevated temperature environments. The data identifies 298.15 K as a critical thermal threshold where coupling nonlinearity undergoes regime transition, transforming manageable pressure responses into potentially hazardous conditions. This threshold behavior suggests that THMC coupling exhibits bistable characteristics, where small temperature increments beyond critical values trigger disproportionate system responses due to positive feedback mechanisms between thermal, hydraulic, and mechanical processes. The scaling relationships establish that temperature-controlled coring protocols must prioritize pressure containment over process acceleration, as the exponential nature of pressure scaling overwhelms the moderate benefits of enhanced dissociation rates at elevated temperatures.

6. Conclusions

This study investigates temperature-driven THMC coupling mechanisms in NGH cores through fully coupled

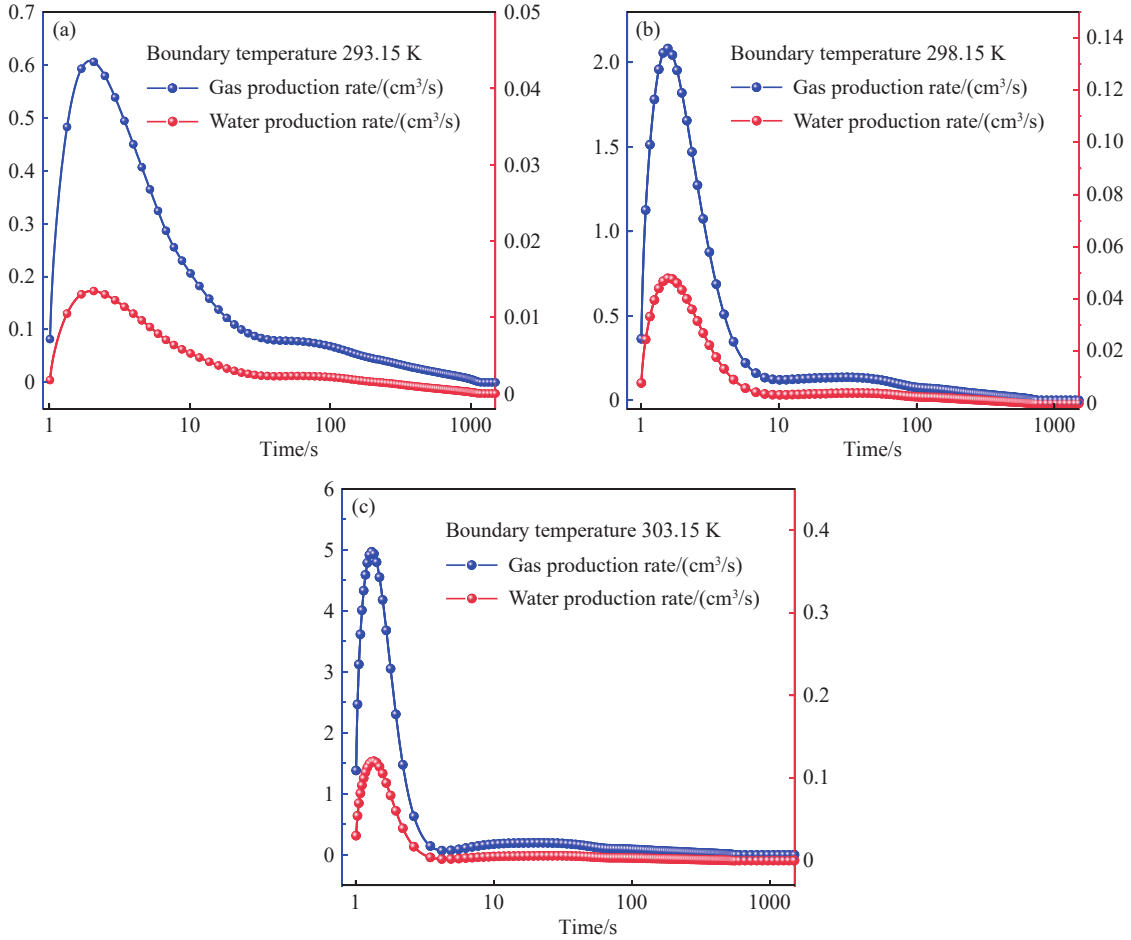

Fig. 14. Time-logarithmic curves of gas and water production rates at the upper surface of the core under *in-situ* pressure conditions and different temperature boundary conditions: a–293.15 K; b–298.15 K; c–303.15 K.

numerical simulation. Numerical experiments at temperature boundaries (293.15–303.15 K) reveal complex feedback relationships between thermal disturbances and hydrate core stability.

(i) Temperature field evolution exhibits exponential growth characteristics generating radial gradients of 8–35 K/cm, triggering pressure surges from 0.11 MPa to 0.82 MPa through stepwise propagation mechanisms and establishing intense positive feedback loops that destabilize hydrate structures.

(ii) Hydrate dissociation follows "S-shaped decay" patterns with 2 times rate acceleration under elevated temperatures, reducing completion time from 1200 s to 600 s through three stages of heat conduction-controlled processes.

(iii) Relative permeability demonstrates critical "threshold effects" with explosive growth exceeding three orders of magnitude when hydrate saturation drops below 0.15–0.2, indicating distinct percolation phenomena that fundamentally transform hydraulic properties.

(iv) Multiphase fluid migration evolves from slow diffusion (0–0.4×10^{-3} m/s) to explosive patterns (1×10^{-3}–1.25×10^{-3} m/s), exhibiting characteristic "burst-decay" kinetics and spatial differentiation with pronounced viscous fingering phenomena.

(v) Under unconfined conditions, macroscopic deformation remains negligible while porosity evolution becomes the critical structural parameter controlled by pressure-driven pore expansion mechanisms distinct from conventional consolidation theory.

These findings quantify THMC coupling mechanisms during temperature-driven hydrate dissociation in pressure-preserved cores. However, current assumptions neglect three-dimensional effects including circumferential heterogeneity, anisotropic stress distributions, and complex fracture networks. Natural multi-component hydrate systems mixtures exhibit distinct dissociation characteristics requiring component-specific phase equilibria and competitive kinetics modeling. Addressing these research directions through advanced numerical schemes, wellbore-formation coupling, and real-time monitoring protocols will enhance pressure-preserved coring technology toward reliable field applications.

CRediT authorship contribution statement

Meng Xu: Data curation and writing original draft preparation; Ya-chen Xie: data curation, visualization and investigation; Le Zhao: data curation, editing and supervision; Ling Chen: reviewing and editing; Chao Yuan: validation;

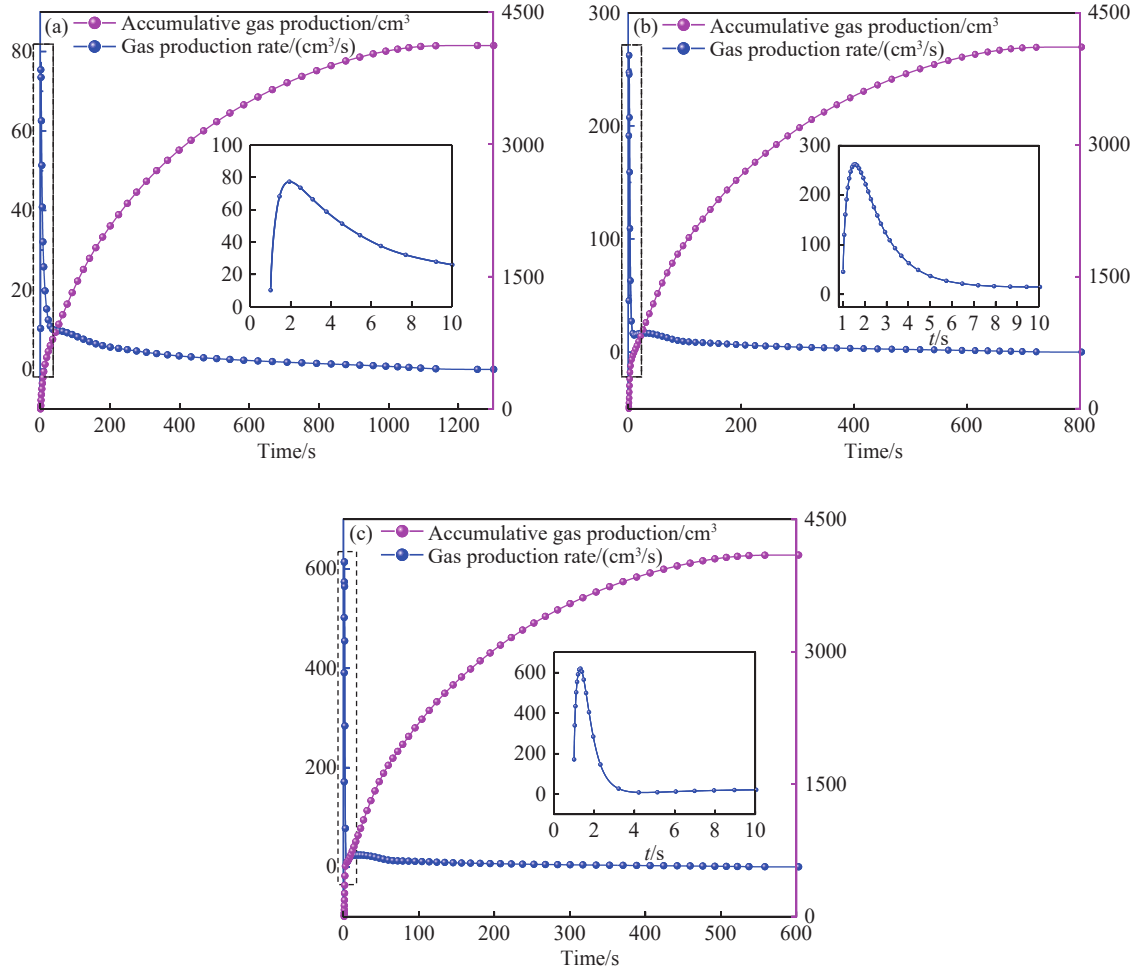

Fig. 15. Gas production rate and cumulative gas production at standard temperature and pressure conditions on the upper surface of the core under different temperature boundary conditions: a–293.15 K; b–298.15 K; c–303.15 K.

Table 5. Comprehensive comparison of key parameters under different temperature boundary conditions in core geometric center.

Parameter	293.15 K	298.15 K	303.15 K
Dissociation completion time/s	1157	737	543
Maximum pressure gradient/(MPa/mm)	0.15	0.52	1.24
Peak overpressure/MPa	0.11	0.38	0.82
Maximum gas saturation	0.61	0.69	0.73
Critical pressure buildup rate/(MPa/s)	0.018	0.089	0.205

Jia-liang Chen: reviewing and editing; Cheng-hang Fu: reviewing and editing; Han Wu: reviewing and editing; Gui-kang Liu: reviewing and editing; Ming-zhu Qi: reviewing and editing; Ming Zhang: reviewing and editing; He-ping Xie: conceptualization and methodology.

Declaration of competing interest

The authors declare no conflicts of interest.

Acknowledgment

This research was financially supported by Shenzhen Science and Technology Program (KJZD20231025152759002, JSGG20220831105002005). The authors would like to express their gratitude for the support provided by the National Natural Science Fund Foundation of China (52374357, 523B2101).

Data availability

The data that support the findings of this study are available from the corresponding author upon reasonable request.

Supplementary dataset

Supplementary data (Appendix A and B) to this article can be found online at doi: 10.31035/cg2025257.

References

Amann H, Hohnberg H, Reinelt R. 1997. HYACE–a novel autoclave coring equipment for systematic offshore gas hydrate sampling. https://www.osti.gov/etdeweb/biblio/613946.

Bohrmann G, Trehu AM, Baldauf J, Richter C. 2002. Ocean Drilling Program Leg 204 Scientific Prospectus Drilling Gas Hydrates On Hydrate Ridge, Cascadia Continental Margin. College Station,

Taxas, 50. https://brg.ldeo.columbia.edu/data/odp/odp-log_sum/leg204/204.index.html.

Collett TS, Riedel M, Boswell R, Presley J, Kumar P, Sathe A, Sethi A, Lall M, Scientists NE. 2015. Indian national gas hydrate program expedition 01 report (2328–0328). doi: 10.3133/sir20125054.

Dai S, Boswell R, Waite W, Jang J, Lee JY, Seol Y. 2017. What has been learned from pressure cores. https://www.netl.doe.gov/sites/default/files/netl-file/Dai-et-al-ICGH-2017.pdf.

Dai S, Santamarina JC. 2014. Sampling disturbance in hydrate-bearing sediment pressure cores: NGHP-01 expedition, Krishna–Godavari Basin example. Marine and Petroleum Geology, 58, 178–186. doi: 10.1016/j.marpetgeo.2014.07.013.

Dickens GR, Wallace PJ, Paull CK, Borowski WS. 2000. Detection of methane gas hydrate in the pressure core sampler (PCS): Volume-pressure-time relations during controlled degassing experiments. Proceedings of the Ocean Drilling Program: Scientific Results. doi: 10.2973/odp.proc.sr.164.245.2000.

Gershenzon NI, Ritzi Jr RW, Dominic DF, Mehnert E, Okwen RT. 2016. Comparison of CO_2 trapping in highly heterogeneous reservoirs with Brooks-Corey and van Genuchten type capillary pressure curves. Advances in Water Resources, 96, 225–236. doi: 10.1016/j.advwatres.2016.07.022.

Guo XY, Jin Y, Zi JY, Lin JY, Zhu BL. 2023. A 3D modeling study of effects of heterogeneity on system responses in methane hydrate reservoirs with horizontal well depressurization. Gas Science and Engineering, 115, 205001. doi: 10.1016/j.jgsce.2023.205001.

Hong H, Pooladi-Darvish M, Bishnoi PR. 2003. Analytical modelling of gas production from hydrates in porous media. Journal of Canadian Petroleum Technology, 42(11), 45–56. doi: 10.2118/03-11-05.

Inada N, Yamamoto K. 2015. Data report: Hybrid Pressure Coring System tool review and summary of recovery result from gas-hydrate related coring in the Nankai Project. Marine and Petroleum Geology, 66, 323–345. doi: 10.1016/j.marpetgeo.2015.02.023.

Ji YK, Kneafsey TJ, Hou J, Zhao JL, Liu CL, Guo TK, Wei B, Zhao EM, Bai YJ. 2022. Relative permeability of gas and water flow in hydrate-bearing porous media: A micro-scale study by lattice Boltzmann simulation. Fuel, 321, 124013. doi: 10.1016/j.fuel.2022.124013.

Kamath VA. 1984. Study of heat transfer characteristics during dissociation of gas hydrates in porous media. University of pittsburgh. https://www.scirp.org/reference/referencespapers?referenceid=2253843.

Kim HC, Bishnoi PR, Heidemann RA, Rizvi SSH. 1987. Kinetics of methane hydrate decomposition. Chemical Engineering Science, 42(7), 1645–1653. doi: 10.1016/0009-2509(87)80169-0.

Kuang YM, Yang L, Li QP, Lv X, Li YP, Yu B, Leng SD, Song YC, Zhao JF. 2019. Physical characteristic analysis of unconsolidated sediments containing gas hydrate recovered from the Shenhu Area of the South China sea. Journal of Petroleum Science and Engineering, 181, 106173. doi: 10.1016/j.petrol.2019.06.037.

Kubo Y, Mizuguchi Y, Inagaki F, Yamamoto K. 2014. A new hybrid pressure-coring system for the drilling vessel Chikyu. Scientific Drilling, 17, 37–43. doi: 10.5194/sd-17-37-2014.

Kvenvolden KA, Cameron DH. 1983. Pressure core barrel: Application to the study of gas hydrates, Deep Sea Drilling Project Site 533, Leg 76. Initial Reports of the DSDP, 76, 367–375. doi: 10.2973/dsdp.proc.76.107.1983.

Leverett MC. 1941. Capillary behavior in porous solids. Transactions of the AIME, 142(1), 152–169. doi: 10.2118/941152-G.

Li CH, Zhao Q, Xu HJ, Feng K, Liu XW. 2014. Relation between relative permeability and hydrate saturation in Shenhu area, South China Sea. Applied Geophysics, 11(2), 207–214. doi: 10.1007/s11770-014-0432-6.

Li J, Lu JA, Kang DJ, Ning FL, Lu HF, Kuang ZG, Wang DD, Liu CL, Hu GW, Wang JS, Liang JQ. 2019. Lithological characteristics and hydrocarbon gas sources of gas hydrate-bearing sediments in the Shenhu area, South China Sea: Implications from the W01B and W02B sites. Marine Geology, 408, 36–47. doi: 10.1016/j.margeo.2018.10.013.

Li Y, Xu CL, Zhu JX, Lu HF, Liu YT, Gu YH, Pan ZJ, Linga P, Yin ZY. 2024. Comprehensive characterizations of core sediments recovered from Shenhu W17 well in South China Sea and its impact on methane hydrate kinetics. Gas Science and Engineering, 131, 205482. doi: 10.1016/j.jgsce.2024.205482.

Li YL, Wu NY, Wang HB, Ji YK, Qi MH, Liu CL, Wan YZ, Chen MT. 2024. Multi-field coupling modes during marine natural gas hydrate exploitation and its advancements. Journal of Engineering Geology, 32(4), 1355–1366 (in Chinese with Eglish abstract). doi: 10.13544/j.cnki.jeg.2023-0260.

Liang W, Wang JG, Li PB. 2022. Gas production analysis for hydrate sediment with compound morphology by a new dynamic permeability model. Applied Energy, 322, 119434. doi: 10.1016/j.apenergy.2022.119434.

Liu CL, Ye YG, Meng QG, He XL, Lu HL, Zhang J, Liu J, Yang SX. 2012. The characteristics of gas hydrates recovered from Shenhu Area in the South China Sea. Marine Geology, 307, 22–27. doi: 10.1016/j.margeo.2012.03.004.

Lu C, Qin XW, Ma C, Yu L, Geng LT, Bian H, Zhang KN, Zhou YF. 2022. Investigation of the impact of threshold pressure gradient on gas production from hydrate deposits. Fuel, 319, 123569. doi: 10.1016/j.fuel.2022.123569.

Lu QP, Qin RL, Yu YJ, Qi LQ, Xie WW, Lu HF, Xu BC, Shi HX, Xu CL, Li XC. 2024. The design and application of a new wireline pressure coring system for the Guangzhou marine geological survey methane hydrate expedition in the South China Sea. Applied Sciences, 14(15), 6753. doi: 10.3390/app14156753.

Ma TR, Rutqvist J, Oldenburg CM, Liu WQ, Chen JG. 2017. Fully coupled two-phase flow and poromechanics modeling of coalbed methane recovery: Impact of geomechanics on production rate. Journal of Natural Gas Science and Engineering, 45, 474–486. doi: 10.1016/j.jngse.2017.05.024.

Qin XW, Lu C, Wang PK, Liang QY. 2022. Hydrate phase transition and seepage mechanism during natural gas hydrates production tests in the South China Sea: A review and prospect. China Geology, 5(2), 201–217. doi: 10.31035/cg2022029.

Qin XW, Lu JA, Lu HL, Qiu HJ, Liang JQ, Kang DJ, Zhan LS, Lu HF, Kuang ZG. 2020. Coexistence of natural gas hydrate, free gas and water in the gas hydrate system in the Shenhu Area, South China Sea. China Geology, 3(2), 210–220. doi: 10.31035/cg2020038.

Rabinowitz PD, Garrison L, Herrig S, Kidd RB, McLerran AR, Merrell WJ, Olivas R, Meyer AW. 1985. Scientific ocean drilling: An overview of the ocean drilling program. Offshore Technology Conference, May 6−9, 1985. Houston, Texas, USA. doi: 10.4043/4989-MS.

Schultheiss P, Holland M, Humphrey G. 2009. Wireline coring and analysis under pressure: Recent use and future developments of the HYACINTH system. Scientific Drilling, 7, 44–50. doi: 10.2204/iodp.sd.7.07.2009.

Schultheiss P, Holland M, Roberts J, Bigalke N, Mimitz M. 2017. Advances in wireline pressure coring, core handling, and core analysis related to gas hydrate drilling investigations. Proceedings of the 9th International Conference on Gas Hydrates (ICGH 2017),

Sloan ED. 2003. Fundamental principles and applications of natural gas hydrates. Nature, 426(6964), 353–359. doi: 10.1038/nature02135.

Sloan ED, Koh CA. 2008. Clathrate Hydrates of Natural Gases. Boca Raton, CRC Press, 1–752. doi: 10.1201/9781420008494.

Waite WF, Ruppel CD, Boze L, Lorenson TD, Buczkowski BJ, McMullen KY, Kvenvolden KA. 2020. Preliminary global database of known and inferred gas hydrate locations. U.S. Geological Survey data release. doi: 10.5066/P9LLFVJM.

Wakishima R. 1998. The development of a pressure temperature core sampler (PTCS) for the recovery of in-situ methane hydrates. Proceedings of the International Symposium on Methane Hydrates. https://cir.nii.ac.jp/crid/1571417124654349952.

Wan Y, Wu N, Chen Q, Li W, Hu G, Huang L, Ouyang W. 2022. Coupled thermal-hydrodynamic-mechanical–chemical numerical simulation for gas production from hydrate-bearing sediments based on hybrid finite volume and finite element method. Computers and Geotechnics, 145, 104692. doi: 10.1016/j.compgeo.2022.104692.

Wang H, Li Y, Huang L, Liu T, Liu W, Wu P, Song Y. 2024. A pore-scale study on microstructure and permeability evolution of hydrate-bearing sediment during dissociation by depressurization. Fuel, 358, 130124. doi: 10.1016/j.fuel.2023.130124.

Wang JG, Peng Y. 2014. Numerical modeling for the combined effects of two-phase flow, deformation, gas diffusion and CO_2 sorption on caprock sealing efficiency. Journal of Geochemical Exploration, 144, 154–167. doi: 10.1016/j.gexplo.2013.12.011.

Wang XJ, Collett TS, Lee MW, Yang SX, Guo YQ, Wu SG. 2014. Geological controls on the occurrence of gas hydrate from core, downhole log, and seismic data in the Shenhu area, South China Sea. Marine Geology, 357, 272–292. doi: 10.1016/j.margeo.2014.09.040.

Wei JG, Liang JQ, Lu JG, Zhang W, He YL. 2019. Characteristics and dynamics of gas hydrate systems in the northwestern South China Sea-Results of the fifth gas hydrate drilling expedition. Marine and Petroleum Geology, 110, 287–298. doi: 10.1016/j.marpetgeo.2019.07.028.

Wei JG, Yang L, Liang QY, Liang JG, Lu JG, Zhang W, Zhang XH, Lu XB. 2021. Geomechanical properties of gas hydrate-bearing sediments in Shenhu area of the South China Sea. Energy Reports, 7, 8013–8020. doi: 10.1016/j.egyr.2021.05.063.

Wu NY, Yang SX, Zhang HQ, Liang JQ, Wang HB, Lu JA. 2010. Gas hydrate system of Shenhu area, northern South China Sea: Wire-line logging, geochemical results and preliminary resources estimates. Offshore Technology Conference. May 3−6, 2010. Houston, Texas, USA. doi: 10.4043/20485-MS.

Xu M, Xie YC, Zhao L, Yuan C, Chen L, Chen JL, Liu GK, Qi MZ, Zhang M, Xie HP. 2026. Coring and analysis technologies for natural gas hydrate reservoirs: Achievements, obstacles, and future directions. Fuel, 404, 136027. doi: 10.1016/j.fuel.2025.136027.

Youslf MH, Abass HH, Selim MS, Sloan ED. 1991. Experimental and theoretical investigation of methane-gas-hydrate dissociation in porous media. SPE Reservoir Engineering, 6(1), 69–76. doi: 10.2118/18320-PA.

Yu YS, Zhang XW, Liu JW, Lee Y, Li XS. 2021. Natural gas hydrate resources and hydrate technologies: A review and analysis of the associated energy and global warming challenges. Energy & Environmental Science, 14(11), 5611–5668. doi: 10.1039/D1EE02093E.

Zhang LM, Zhang CD, Zhang K, Zhang L., Yao J, Sun H, Yang YF. 2019. Pore-scale investigation of methane hydrate dissociation using the lattice Boltzmann method. Water Resources Research, 55(11), 8422–8444. doi: 10.1029/2019WR025195.

Zhang RW, Lu JG, Wen PF, Kuang ZG, Zhang BJ, Xue H, Xu YX, Chen X. 2018. Distribution of gas hydrate reservoir in the first production test region of the Shenhu area, South China Sea. China Geology, 1(4), 493–504. doi: 10.31035/cg2018049.

Zhang Y, Zhao J, Bhattacharjee G, Xu HZ, Yang MJ, Kumar R, Linga P. 2022. Synthesis of methane hydrate at ambient temperature with ultra-rapid formation and high gas storage capacity. Energy & Environmental Science, 15(12), 5362–5378. doi: 10.1039/D2EE01968J.